Large-Gap Quantum Spin Hall State in MXenes: *d*-Band Topological Order in a Triangular Lattice

Chen Si,[†,‡] Kyung-Hwan Jin,[§] Jian Zhou,[†] Zhimei Sun,*[,†,‡] and Feng Liu[§]

[†]School of Materials Science and Engineering, Beihang University, Beijing 100191, China

[‡]Center for Integrated Computational Materials Engineering, International Research Institute for Multidisciplinary Science, Beihang University, Beijing 100191, China

[§]Department of Materials Science and Engineering, University of Utah, Salt Lake City, Utah 84112, United States

Ⓢ Supporting Information

ABSTRACT: MXenes are a large family of two-dimensional (2D) early transition metal carbides that have shown great potential for a host of applications ranging from electrodes in supercapacitors and batteries to sensors to reinforcements in polymers. Here, on the basis of first-principles calculations, we predict that $Mo_2MC_2O_2$ (M = Ti, Zr, or Hf), belonging to a recently discovered new class of MXenes with double transition metal elements in an ordered structure, are robust quantum spin Hall (QSH) insulators. A tight-binding (TB) model based on the d_{z^2}-, d_{xy}-, and $d_{x^2-y^2}$-orbital basis in a triangular lattice is also constructed to describe the QSH states in $Mo_2MC_2O_2$. It shows that the atomic spin−orbit coupling (SOC) strength of M totally contributes to the topological gap at the Γ point, a useful feature advantageous over the usual cases where the topological gap is much smaller than the atomic SOC strength based on the classic Kane−Mele (KM) or Bernevig−Hughes−Zhang (BHZ) model. Consequently, $Mo_2MC_2O_2$ show sizable gaps from 0.1 to 0.2 eV with different M atoms, sufficiently large for realizing room-temperature QSH effects. Another advantage of $Mo_2MC_2O_2$ MXenes lies in their oxygen-covered surfaces which make them antioxidative and stable upon exposure to air.

KEYWORDS: *MXene, topological insulator, large gap, triangular lattice, first-principles calculations*
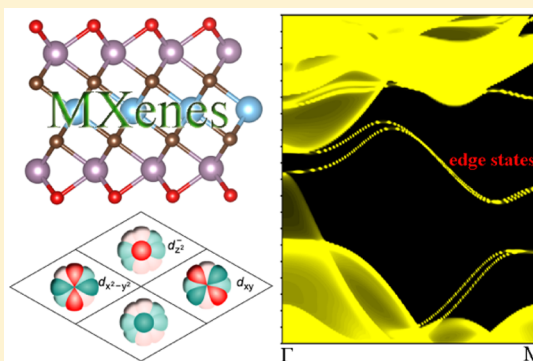
MXenes, a large family of 2D transition metal (TM) carbides, have attracted considerable attention in the past few years due to their promising applications in Li-ion batteries, supercapacitors, sensors, and catalysis.[1] MXenes are produced by selectively etching of "A" layers from their 3D layered parent compounds, the MAX phases with a general formula of $M_{n+1}AX_n$, where M is an early TM, A is mainly a group IIIA or IVA element, X is C or/and N, and n = 1, 2, 3.[2] Experimentally MXenes containing a single TM element, such as Ti_2C, V_2C, Nb_2C, Ti_3C_2, Ta_4C_3, and Nb_4C_3 were first synthesized.[1] Very recently, a new class of MXenes which contain double TM elements in a fully ordered structure, such as Mo_2TiC_2 and Cr_2TiC_2, have also been synthesized.[3] So far, MXenes have displayed a wide range of physical properties, such as metallicity with excellent conductivity,[2] semiconductivity with tunable gap,[4] half-metallic ferromagnetism,[5] ultralow work function,[6] large Seebeck coefficients,[4] high flexibility,[7,8] and so on, which opens enticing possibilities of MXenes in various applications.

The QSH effect, hosted in a 2D system of QSH insulators, is a novel quantum state of matter that has an insulating gap in the bulk and gapless states at the edge where opposite spin states counter-propagate.[9] Remarkably, the low-energy scattering of the edge states are completely forbidden by the time reversal symmetry, which offers a promising way to quantum electronic devices without dissipation. Graphene is the first proposed QSH insulator,[10] yet the extremely small bulk gap of 10^{-3} meV makes its QSH effect unobservable.[11,12] Then the QSH effect was theoretically predicted and experimentally observed in the HgTe/CdTe quantum well[13,14] and subsequently in the InAs/GaSb quantum well.[15] However, their bulk gaps are very small (of the order of meV), limiting the operating regime to ultralow temperatures (below 10 K).[14] Many candidates were also proposed, including silicene,[16] heavy atoms Ge, Sn, Pb, Sb, or Bi-based 2D films,[17−27] 2D organometallic frameworks,[28] TM chalcogenides and halides,[29−33] Mn-intercalated graphene-SiC,[34,35] and surface-based 2D topological insulators,[36,37] but none of them has been confirmed experimentally, except Bi(111) bilayer grown on a substrate whose topological edge states have been measured.[38] Thus, the search for new QSH insulators with large gaps that can support high temperature applications is vitally important, especially in existing 2D materials, such as the

large MXene family. We note that very recently W_2CO_2, a oxidized W_2C MXene single layer, was predicted to be a QSH insulator;[39] however, the W-based MAX phases such as W_2AlC are verified to be unstable and have not been successfully produced so far,[40] casting doubt on experimental feasibility of synthesizing W_2CO_2.

In this Letter, we predict a new class of large-gap QSH insulators in 2D ordered, double TM MXenes $Mo_2MC_2O_2$ (M = Ti, Zr, or Hf), where O is the surface functional group. Among them, $Mo_2TiC_2O_2$ may be readily made by the present synthesis method.[3,41] First-principles calculations of band structures, Z_2 topological invariants and edge states as well as a TB model based on the d_{z^2}-, d_{xy}-, and $d_{x^2-y^2}$-orbital basis in a triangular lattice are used to reveal the nontrivial topological properties of $Mo_2MC_2O_2$. There are three important advantages for the QSH states discovered in $Mo_2MC_2O_2$. First, the topological orders in MXenes represent a new class of d-band QSH phase in a triangular lattice, which extends the search of QSH insulators from honeycomb and square lattices to triangular lattices and hence will greatly broaden the scope of topological materials. Second, the TB model shows that the atomic SOC strength of M totally contributes to the topological gap at the Γ point, which gives rise to sizable topological gaps from 0.1 to 0.2 eV for $Mo_2MC_2O_2$ depending on the choice of M atoms. In contrast, the topological gap is much smaller than the atomic SOC strength in those systems predicted based on the classic KM[10] or BHZ model.[13,14] Third, MXenes are usually fabricated by immersing MAX powers in acidic solutions, so the surfaces of MXenes are inevitably terminated by primarily O and/or OH groups,[41,42] and the latter can be converted into O termination by high temperature annealing[41] or by metal adsorption.[41,43] Thus, the $Mo_2MC_2O_2$ systems having fully oxidized surfaces are naturally stable against surface oxidation and degradation, makes them more promising for practical applications.

Lattice Structures of 2D $Mo_2MC_2O_2$ Systems. Bare Mo_2MC_2 (M = Ti, Zr, or Hf) MXene has a 2D hexagonal structure with the space group P-3M1 (see Figure 1). It consists
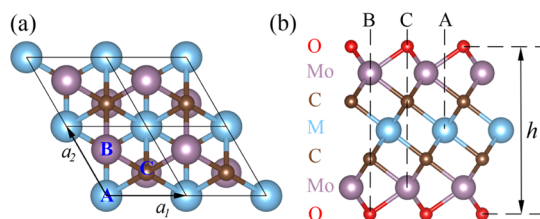

Figure 1. (a) Top view of the crystal structure of Mo_2MC_2 (M = Ti, Zr, or Hf) MXene displaying the hexagonal unit cell with Bravais lattice vectors a_1 and a_2. (b) Side view of the crystal structure of $Mo_2MC_2O_2$. h denotes the thickness of septuple atomic layers of $Mo_2MC_2O_2$.

of five atomic layers stacked in a sequence of Mo−C−M−C−Mo; i.e., it has a fully ordered configuration wherein a M layer is sandwiched between two outer Mo carbide layers.[3] In each atomic layer, the atoms are arranged in a triangular sublattice. It has been known that the present synthesis procedures (etching A layers from the bulk MAX phase in acidic solutions to obtain MXene) lead to the termination of MXene surfaces by mainly O and OH groups.[41,42] As a consequence, the chemistry of exfoliated MXene is expected to be functionalized MXene rather than the bare material. Given that by high temperature

annealing, the OH groups on MXene surfaces are also converted to O termination,[41] we therefore consider the functionalized MXene with surfaces fully terminated by O, which requires two O atoms per unit cell, with one on the top surface and the other on the bottom surface. As shown in Figure 1a, the O atoms might occupy three different sites, namely, A, B, and C, on each surface of Mo_2MC_2. Consequently, there are six inequivalent combinations for decorating the two surfaces, as listed in Supplementary Table S1. For each case, the crystal structure of the oxidized Mo_2MC_2 ($Mo_2MC_2O_2$) is fully optimized, and the calculated relative total energy is presented in Table S1. It is shown that the CB-type surface oxidization is energetically most stable for all three systems, with both surfaces O atoms being located on the top of the nearest C atoms (see Figure 1b). The lattice constants (a) and thickness (h) of all of the 2D $Mo_2MC_2O_2$ (M = Mo, Zr, or Hf) crystals are summarized in Table 1. Given the crystal

Table 1. Lattice Constants (a), Thickness (h), Nontrivial Gaps at the Γ Point (E_Γ), Indirect Bulk Gaps (E_{bulk}), and Z_2 Topological Invariants for $Mo_2MC_2O_2$[a]

compound		$Mo_2TiC_2O_2$	$Mo_2ZrC_2O_2$	$Mo_2HfC_2O_2$
a (Å)		2.94	3.02	3.01
h (Å)		7.59	7.79	7.75
E_Γ (eV)	GGA	0.052	0.087	0.213
	HSE06	0.125	0.147	0.301
E_{bulk} (eV)	GGA	0.041	0.066	0.154
	HSE06	0.096	0.105	0.201
Z_2		1	1	1

[a]The values of E_Γ and E_{bulk} calculated by GGA and HSE06 are all shown for comparison.

structures of $Mo_2MC_2O_2$, we have calculated their phonon spectra to test the structural stability, as shown in Supplementary Figure S2. No negative frequencies are found at any wavevector, demonstrating the dynamic stability of 2D $Mo_2MC_2O_2$.

Electronic and Topological Properties of $Mo_2MC_2O_2$. We next focus on the electronic structures of $Mo_2MC_2O_2$. Both GGA and GGA + SOC band structures of $Mo_2MC_2O_2$ are shown in Figure 2. Without SOC, the three $Mo_2MC_2O_2$ systems are gapless with the valence and conduction bands degenerate at the Γ point, mainly composed of $M-d_{xy,x^2-y^2}$ orbitals, as shown by the partial band projections in Figure 2. With SOC, the doubly degenerate $M-d_{xy,x^2-y^2}$ orbitals split at the Γ point into two states, resulting in a finite energy gap. To identify the topological nature of the insulating phases and since the system possesses inversion symmetry, following the method by Fu and Kane,[44] the topological invariant Z_2 is calculated from wave functions for all occupied bands at four time-reversal invariant k points [i.e., (0, 0, 0), (0.5, 0, 0), (0, 0.5, 0), and (0.5, 0.5, 0) points]. Z_2 is obtained to be 1 for all three $Mo_2MC_2O_2$ systems, indicating they are QSH insulators. We also calculated the band structures using hybrid density functionals (HSE06) (see Supporting Information, Figure S3), which confirmed our above findings from the GGA results as shown in Figure 2, except with larger gaps.

It is widely known that one remarkable characteristic for QSH insulators is the existence of gapless edge states inside the bulk gap. Thus, we have calculated edge states of $Mo_2MC_2O_2$ using the Wannier90 package[45] and a TB Hamiltonian in the basis of the maximally localized Wannier functions (MLWFs)
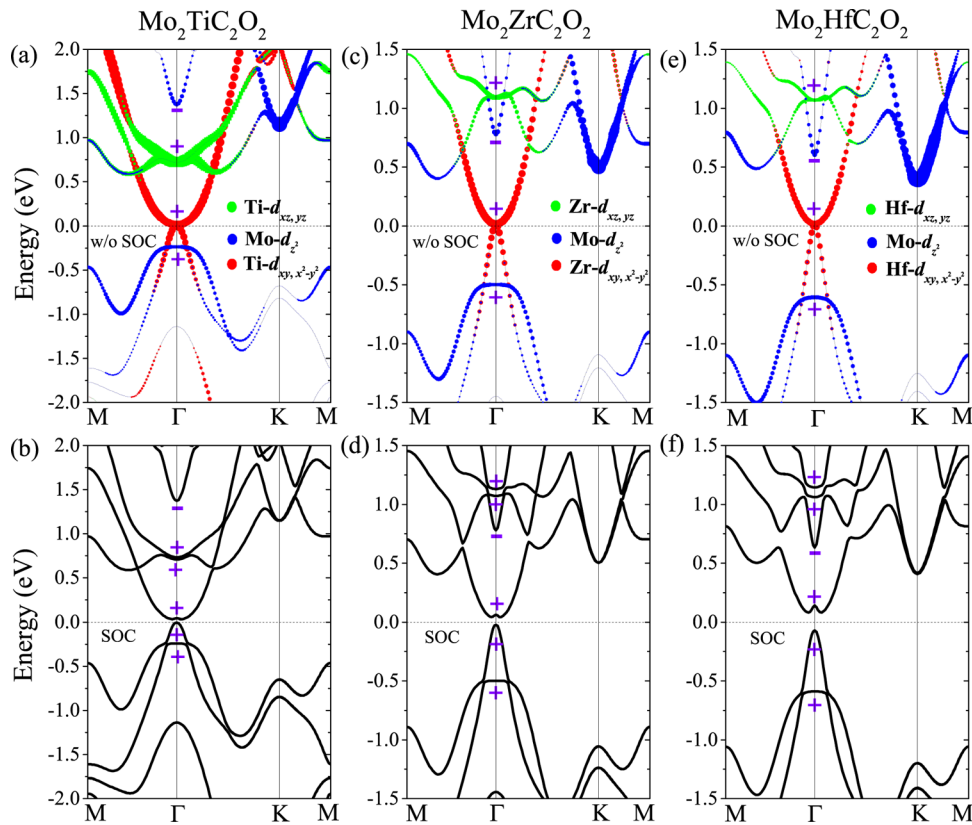
Figure 2. Calculated GGA band structures for $Mo_2TiC_2O_2$ (a, b), $Mo_2ZrC_2O_2$ (c, d), and $Mo_2HfC_2O_2$ (e, f) with and without SOC. The upper panels (a, c, e) are calculated without SOC, while the lower panels (b, d, f) are calculated with SOC. The Fermi level is set to zero. Parities of the Bloch states at the Γ point are denoted by +, −.

fitted to the first-principles band structures.[46] Using the MLWFs, the edge Green's function of the semi-infinite $Mo_2MC_2O_2$ lattice is constructed whose imaginary part gives the local density of states (LDOS), from which we obtained the energy dispersion of the edge states. Figure 3 displays the LDOS on the zigzag edge of $Mo_2HfC_2O_2$, a pair of topological edges states are clearly seen to connect the bulk conduction and valence bands to form a single Dirac cone at the M point. Similar results are found for $Mo_2TiC_2O_2$ and $Mo_2ZrC_2O_2$.

The Mechanism for the QSH Phase. In $Mo_2MC_2O_2$, the effect of SOC is to directly open the nontrivial bulk gap but not

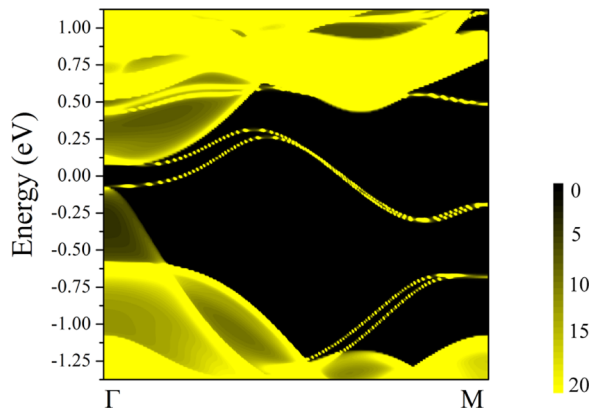**Figure 3.** Energy and momentum-dependent local density of states for $Mo_2HfC_2O_2$ on the zigzag edge, with the Fermi level set to zero. The edge states form a single Dirac cone at the M point and connect the bulk valence and conduction bands.

for inducing band inversion. Like some QSH insulators such as GeI[17] and SnI,[19] $Mo_2MC_2O_2$ has already possessed inverted band ordering without SOC. Taking $Mo_2HfC_2O_2$ as an example, we examined the band structure evolution at the Γ point by analyzing the band order associated with atomic orbitals. Under the D_{3d} symmetry of the crystal group, five d orbitals of each TM atom are split into a single d_z^2 orbital and two doubly degenerate d_{xy, x^2-y^2} and $d_{xz, yz}$ orbitals. According to the partial band projections in Figure 2e, it is clear that the electronic states around the Fermi level (E_F) are mainly contributed to the Hf−d_{xy, x^2-y^2} and Mo−d_z^2 orbitals, so we reasonably neglect other atomic orbitals in the following discussion. It is noted that there are two Mo atoms in one unit cell. As presented in Figure 4a, the two d_z^2 orbitals from the two Mo atoms form bonding and antibonding states, labeled as |Mo−$d_{z^2}^+$⟩ and |Mo−$d_{z^2}^-$⟩, respectively, where the superscript + (−) denotes the even (odd) parity. And the band inversion occurs between the |Hf−$d_{xy,x^2-y^2}^+$⟩ state and the |Mo−$d_{z^2}^-$⟩ state, which is topologically nontrivial due to the opposite parities. Without SOC, the |Hf−$d_{xy,x^2-y^2}^+$⟩ state is doubly degenerate at the E_F, accordingly the system is a zero-gap semiconductor. With SOC, the |Hf−$d_{xy,x^2-y^2}^+$⟩ state splits into two non-degenerate states, namely, |Hf−$d_{xy+ix^2-y^2,\uparrow}^+$ $d_{xy-ix^2-y^2,\downarrow}^+$⟩ and |Hf−$d_{xy-ix^2-y^2,\uparrow}^+$$d_{xy+ix^2-y^2,\downarrow}^+$⟩, leading to the opening of a nontrivial gap. Similar $d-d$ band inversion was also found in W_2CO_2 discussed before.[39]

To illustrate the band inversion process explicitly, we keep the lattice constant a of 2D $Mo_2HfC_2O_2$ being constant but artificially increase its thickness (h) by uniformly enlarging the vertical distance between neighboring atomic layers while
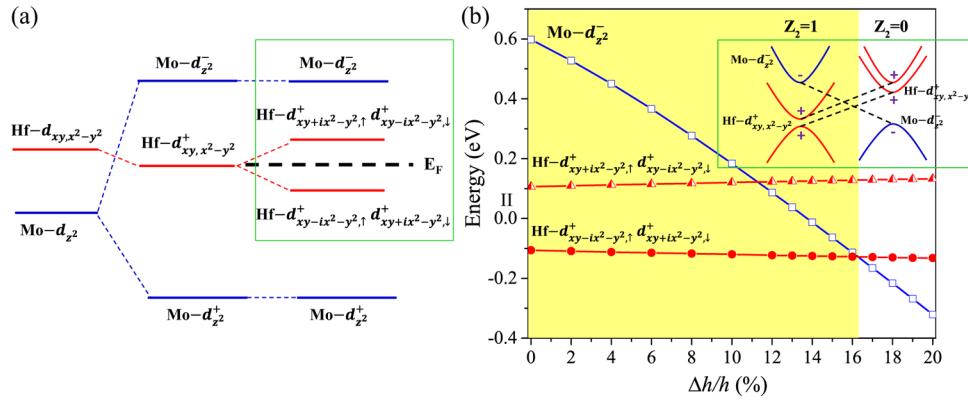
Figure 4. (a) Schematic diagram of the band evolution of $Mo_2HfC_2O_2$ at the Γ point. (b) The relative shift of energy levels $|Mo-d_{z^2}^-\rangle$, $|Hf-d_{xy+ix^2-y^2,\uparrow}^+ d_{xy-ix^2-y^2,\downarrow}^+\rangle$ and $|Hf-d_{xy-ix^2-y^2,\uparrow}^+ d_{xy+ix^2-y^2,\downarrow}^+\rangle$ with the increase of the thickness (h) of $Mo_2HfC_2O_2$. The center of $|Hf-d_{xy+ix^2-y^2,\uparrow}^+ d_{xy-ix^2-y^2,\downarrow}^+\rangle$ and $|Hf-d_{xy-ix^2-y^2,\uparrow}^+ d_{xy+ix^2-y^2,\downarrow}^+\rangle$ is defined as the energy zero. Inset: A schematic representation for the resultant band inversion.
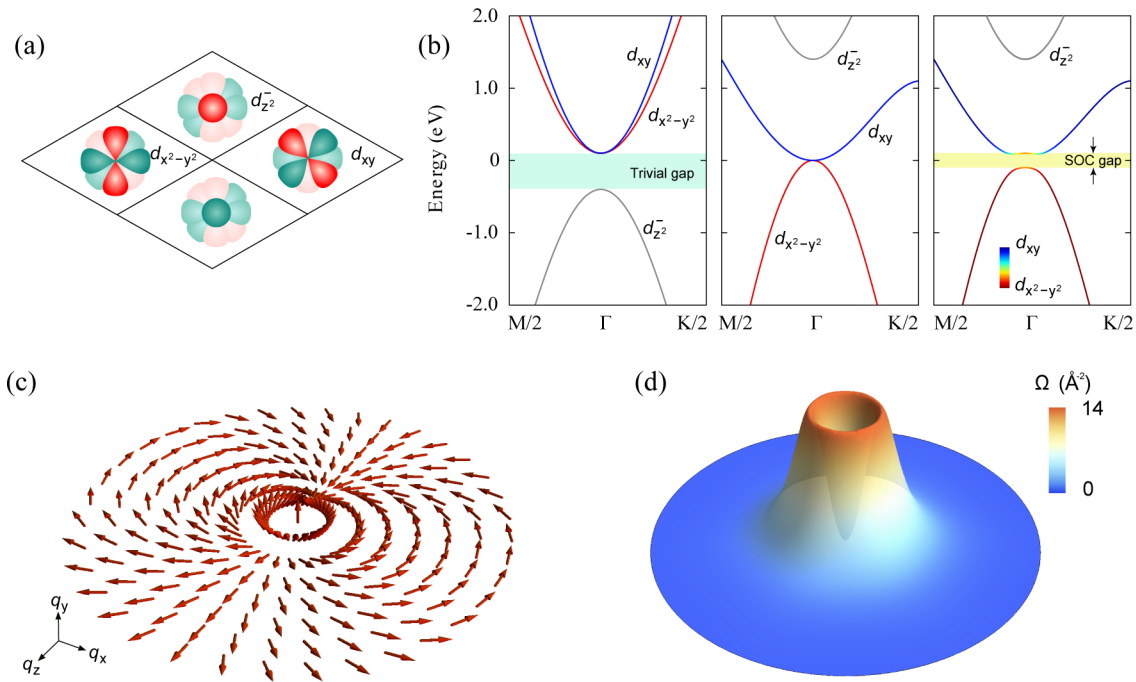

Figure 5. (a) Triangular lattice with three orbitals ($d_{z^2}^-$, d_{xy}, $d_{x^2-y^2}$) per lattice site. The primitive lattice vectors are chosen as $\vec{a}_1 = a(\sqrt{3}/2, -1/2)$ and $\vec{a}_2 = a(\sqrt{3}/2, 1/2)$. (b) The TB band structures with parameters: left, $\varepsilon_z = -4.6$ eV, $\varepsilon_d = 4$ eV, $t_{dz\pi} = 1.4$ eV, $t_{ddz} = 0.1$ eV, $t_{dd\sigma} = -0.8$ eV, $t_{dd\pi} = -0.5$ eV and $\lambda = 0$ eV; middle, $\varepsilon_z = 5.6$ eV, $\varepsilon_d = -1.8$ eV, $t_{dz\pi} = -1.4$ eV, $t_{ddz} = 0.1$ eV, $t_{dd\sigma} = 1.6$ eV, $t_{dd\pi} = 1.0$ eV and $\lambda = 0$ eV; right, same as middle except $\lambda = 0.1$ eV. The gray, red, and blue colors indicate the components of $d_{z^2}^-$, d_{xy}, and $d_{x^2-y^2}$ orbital, respectively. (c, d) Vortex structure of $\hat{q}$ and Berry curvature around the Γ point for the effective two-band model.

maintaining the crystal symmetry. As shown in Figure 4b, with the increase of h, the antibonding state $|Mo-d_{z^2}^-\rangle$ shift downward with respect to the $|Hf-d_{xy+ix^2-y^2,\uparrow}^+ d_{xy-ix^2-y^2,\downarrow}^+\rangle$ and $|Hf-d_{xy-ix^2-y^2,\uparrow}^+ d_{xy+ix^2-y^2,\downarrow}^+\rangle$ states (The evolution for the whole band structure is shown in Supplementary Figure S4 for reference). A crossing between the $|Mo-d_{z^2}^-\rangle$ level and the lower $|Hf-d_{xy-ix^2-y^2,\uparrow}^+ d_{xy+ix^2-y^2,\downarrow}^+\rangle$ level occurs at a critical thickness variation $\Delta h/h$ of around 16%. This level crossing leads to a parity exchange between the occupied and unoccupied bands at the Γ point, resulting in a change of Z_2 from 1 to 0, i.e., a topologically nontrivial to trivial phase transition. This also proves that it is indeed the $d-d$ band inversion between $|Hf-d_{xy,x^2-y^2}^+\rangle$ and $|Mo-d_{z^2}^-\rangle$ that is responsible for the nontrivial band topology in the $Mo_2HfC_2O_2$ system at equilibrium.

Similar to $Mo_2HfC_2O_2$, for $Mo_2TiC_2O_2$ ($Mo_2ZrC_2O_2$) as shown in Figure 2a,c, we can clearly observe a band inversion at the Γ point between $|Ti-d_{xy,x^2-y^2}^+\rangle(|Zr-d_{xy,x^2-y^2}^+\rangle)$ and $|Mo-d_{z^2}^-\rangle$. In addition, different from $Mo_2HfC_2O_2$ ($Mo_2ZrC_2O_2$) where $|Mo-d_{z^2}^-\rangle$ is the lowest state higher than $|Hf-d_{xy,x^2-y^2}^+\rangle(|Zr-d_{xy,x^2-y^2}^+\rangle)$ at the Γ point, in $Mo_2TiC_2O_2$, $|Mo-d_{z^2}^-\rangle$ is further lifted to a higher energy rather than being adjacent to $|Ti-d_{xy,x^2-y^2}^+\rangle$ (see Figure 2a); however, this upward movement of $|Mo-d_{z^2}^-\rangle$ in the regime of conduction bands will not change the nontrivial band topology.

Two interesting points are worthy of further investigation concerning the above band inversion mechanism. First, it is the $d-d$ band inversion, which is strikingly different from the conventional band inversion between $s-p$, $p-p$, or $d-p$ orbitals of apparent opposite parities. Second, even more surprising, the

TM atoms are sitting on a triangular lattice, which is generally not known to support QSH phase before. Given that the QSH phase of Mo$_2$MC$_2$O$_2$ arises from the band inversion between |M$-d_{xy,x^2-y^2}^+$⟩ and |Mo$-d_{z^2}^-$⟩ and the splitting of |M$-d_{xy,x^2-y^2}^+$⟩, we can use a minimal basis of three orbitals (Mo$-d_{z^2}^-$ and M$-d_{xy},d_{x^2-y^2}$) to construct a TB model for understanding the QSH phase. Mo and M atoms belong to two different triangular lattice planes, and we found the coupling between the Mo$-d_{z^2}^-$ orbital and M$-d_{xy},d_{x^2-y^2}$ orbitals are negligible. Thus, we can reasonably ignore the hopping between the Mo$-d_{z^2}^-$ and M$-d_{xy},d_{x^2-y^2}$ orbitals along the z direction, i.e., assume the $d_{z^2}^-$, d_{xy}, and $d_{x^2-y^2}$ orbitals in the same triangular lattice plane as shown in Figure 5a. The corresponding spinless TB Hamiltonian for the triangular lattice can be written as

$$H_0 = \sum_\alpha \varepsilon_\alpha c_{0\alpha}^+ c_{0\alpha} + \sum_i \sum_{\alpha,\beta} (t_{0\alpha,i\beta} c_{0\alpha}^+ c_{i\beta} + t_{i\beta,0\alpha} c_{i\beta}^+ c_{0\alpha})$$

(1)

where α, $\beta = d_{z^2}^-$, d_{xy}, $d_{x^2-y^2}$ are the orbital indices, ε_α is the on-site energy, and $t_{0\alpha,i\beta}$ is the nearest-neighbor (NN) hopping parameter. The on-site SOC term can be written as

$$H_{SOC} = -i\lambda(c_{0,d_{x^2-y^2}}^+ c_{0d_{xy}} - c_{0d_{xy}}^+ c_{0d_{x^2-y^2}})s_z$$

(2)

where λ is the atomic SOC strength of M and s_z is the Pauli matrix. Since spin-up and spin-down Hamiltonians are decoupled, without losing generality, we will focus on the spin-up part (one just needs to change λ to $-\lambda$ for the spin-down Hamiltonian). The spin-up Hamiltonian can be represented as

$$H = H_0 + H_{SOC} = \begin{pmatrix} h_{11} & h_{12} & h_{13} \\ h_{12}^* & h_{22} & h_{23} \\ h_{13}^* & h_{23}^* & h_{33} \end{pmatrix} + \begin{pmatrix} 0 & 0 & 0 \\ 0 & 0 & -\lambda i \\ 0 & \lambda i & 0 \end{pmatrix}$$

(3)

with the expression of

$$h_{11} = \varepsilon_z + t_{dz\pi}\left(2\cos\left(\frac{\sqrt{3}}{2}k_x\right)\cos\left(\frac{1}{2}k_y\right) + \cos(k_y)\right)$$

(4)

$$h_{12} = -\sqrt{3}\,t_{ddz}\sin\left(\frac{\sqrt{3}}{2}k_x\right)\sin\left(\frac{1}{2}k_y\right)$$

$$h_{13} = t_{ddz}\left(\cos(k_y) - \cos\left(\frac{\sqrt{3}}{2}k_x\right)\cos\left(\frac{1}{2}k_y\right)\right)$$

$$h_{22} = \varepsilon_d + (3t_{dd\sigma} + t_{dd\pi})\cos\left(\frac{\sqrt{3}}{2}k_x\right)\cos\left(\frac{1}{2}k_y\right)$$
$$+ 2t_{dd\pi}\cos(k_y)$$

$$h_{23} = \sqrt{3}\,(t_{dd\pi} - t_{dd\sigma})\sin\left(\frac{\sqrt{3}}{2}k_x\right)\sin\left(\frac{1}{2}k_y\right)$$

$$h_{33} = \varepsilon_d + (t_{dd\sigma} + 3t_{dd\pi})\cos\left(\frac{\sqrt{3}}{2}k_x\right)\cos\left(\frac{1}{2}k_y\right)$$
$$+ 2t_{dd\sigma}\cos(k_y)$$

where ε_z and ε_d are onsite energies for $d_{z^2}^-$, $d_{xy}/d_{x^2-y^2}$ orbitals, respectively, $t_{dz\pi}$ is the NN hopping parameter between $d_{z^2}^-$ orbitals, t_{ddz} is the NN hopping parameter between $d_{z^2}^-$ and d_{xy}

(or $d_{x^2-y^2}$) orbitals, and $t_{dd\sigma}$ and $t_{dd\pi}$ are NN hopping parameters corresponding to the σ and π bonds formed by d_{xy} and $d_{x^2-y^2}$ orbitals.

At the Γ point, by diagonalizing H, the three eigenvalues are are calculated to be $E_{d_{xy}d_{x^2-y^2}}^{\pm\lambda} = 3t_{dd\pi} + 3d_{dd\sigma} + \varepsilon_d \pm \lambda$ and $E_{d_{z^2}^-} = 3t_{dz\pi} + \varepsilon_z$, respectively. Clearly, the $d_{z^2}^-$ orbital is independent of SOC, and the d_{xy} and $d_{x^2-y^2}$ orbitals are degenerate without SOC and split with SOC, introducing an energy gap

$$\Delta_\Gamma = 2\lambda$$

(5)

The band structure of this Hamiltonian is shown in Figure 5b, which shows typical three bands with proper parameters. For the trivial case, the $d_{z^2}^-$ orbital is below the d_{xy} and $d_{x^2-y^2}$ bands, and there is no band inversion between orbitals. For the nontrival case, the $d_{z^2}^-$ orbital moves to the highest energy level, and the band order has been inverted even without SOC. Moreover, below the $d_{z^2}^-$ orbital, d_{xy} and $d_{x^2-y^2}$ bands touch each other at the Γ point with quadratic band touching. When including SOC, even an infinitesimal value of λ removes the quadratic band touching between the two bands, turning the system into a QSH phase. Furthermore, we introduce an effective model at the continuum limit, which is adiabatically connected to original lattice model (see Part 7 of the Supporting Information for reference). Consequently, the three-band Hamiltonian is reduced to an effective two-band Hamiltonian around the Γ point as $H = q_0 I + \vec{q}\cdot\vec{\sigma}$, where I is the identity and $\vec{\sigma}$ is Pauli matrices. For the nontrivial band topology, $\hat{q} = \vec{q}/|\vec{q}|$ has a vortex structure around the Γ point, as shown in Figure 5c. At Γ, $\hat{q}$ is along the south pole. When k goes away from Γ, $\hat{q}$ changes direction gradually from out-of-plane to in-plane. Generally, a vortex is a topological defect described by the Chern number (C). Using the $\vec{q}$ vector, the Chern number for the spin-up states can be further defined as

$$C_\uparrow = \frac{1}{4\pi}\int dk_x \int dk_y \hat{q}\left(\frac{\partial\hat{q}}{\partial k_x} \times \frac{\partial\hat{q}}{\partial k_y}\right)$$

(6)

We also calculate the Berry curvature as shown in Figure 5d. The Berry curvature is nonzero around the Γ point and gives $C_\uparrow = 1$. Similarly, when spin-down Hamiltonian is considered, we obtain the Chern number for the spin-down sector $C_\downarrow = -1$. So the spin Chern number, defined as the half difference between the Chern number for the spin-up and spin-down sectors, is $C_s = 1/2(C_\uparrow - C_\downarrow) = 1$, directly confirming a nontrivial topological phase.[47]

This QSH model in the triangular lattice is quite different from the KM model[10] for graphene in the honeycomb lattice and the BHZ band inversion model[13,14] derived from narrow-gap semiconductor quantum well in the square lattice. Based on the KM and BHZ models, many QSH insulators with the honeycomb or square lattices are predicted, yet only two semiconductor systems (HgTe/CdTe and InAs/GaSb quantum wells) are experimentally verified for the BHZ model. It is widely known that the honeycomb and square lattices are "open" lattice structures of low coordination, favored by semiconductor elements with directional bonding. However, metal atoms prefer nondirectional bonding and thus are usually arranged in a close-packing triangular lattice. This QSH model in the triangular lattice shown here is hence beyond the previous honeycomb and square lattice models, providing enticing possibility of finding QSH insulators in triangular lattices. Mo$_2$MC$_2$O$_2$ MXenes are such realistic material systems

comprised of stacks of atomic layers with triangular atomic arrangement in each layer.

Moreover, it is noted that in our model the triangular lattice structure and the d_{xy}, $d_{x^2-y^2}$ orbital configuration greatly enhance the effect of SOC. As shown in eq 5, the topological gap at the Γ point is directly dictated by the atomic on-site SOC strength, equaling 2λ. This unique feature is advantageous over the usual cases based on the classic KM or BHZ mode, where the atomic SOC does not directly contribute to the value of topological gap. In the KM model for graphene and similar material systems, due to the single band structure and the honeycomb lattice symmetry, the effect of atomic-scale SOC on the topological gap is tiny, at the level of high-order perturbation theory.[11,12] For example, the topological gap of graphene is $E \approx \xi^2 (4\Delta_\varepsilon)/(9V_{sp\sigma}^2)$, where ξ is the carbon atomic SOC.[12] Clearly, the topological gap of graphene is second order in the carbon atomic SOC;[12] therefore, the gap of graphene is only 10^{-3} meV although carbon has atomic SOC of about 4 meV. In the BHZ model, the topological gap is introduced by the band inversion which usually occurs between two bands with different orbital characters, e.g., the s and p bands. Without considering $s-p$ hybridization, the band inversion will result in the close of the gap at a finite momenta, and then the $s-p$ hybridization will further open a gap whose nature is topologically nontrivial. According to the $k\cdot p$ perturbation theory, the hybridization strength around the Γ point depends linearly on the magnitude of momenta and thus is typically small.[13,14] This is why in the usual QSH insulators whose topological band gaps are based on band inversion, despite the existence of strong atomic SOC, the topological gaps are still very small. Here, in sharp contrast, because the atomic SOC of M directly contributes to the topological gap, $Mo_2MC_2O_2$ MXene shows a quite sizable bulk gap, as shown in Table 1. Moreover, with the increase of the M atomic weight, the strength of M atomic SOC becomes larger, then the bulk gap also increases. From $Mo_2TiC_2O_2$ to $Mo_2ZrC_2O_2$ and to $Mo_2HfC_2O_2$, according to the HSE calculations, the direct gap at the Γ point increases from 0.125 to 0.147 and to 0.301 eV. A similar trend is also found by the GGA calculations, with gap values slightly underestimated.

Correlation Effects, Substrate Effects, and Multilayer MXenes. For TM containing QSH insulators, one may wonder if the correlation effects of d electrons of TM atoms would influence the topological properties of the systems. So we have investigated the correlation effects of d electrons in $Mo_2MC_2O_2$ by employing the GGA+U approach (with the onsite Hubbard U correction). Using different U values from 0 to 5 eV for Mo, Ti, Hf, and Zr atoms, we find that all three $Mo_2MC_2O_2$ systems remain in the nonmagnetic ground states and the nontrivial topological properties persist. However, when the calculations are expanded to $Cr_2MC_2O_2$ (M = Ti, Zr, or Hf) systems which are found with similar lattice structures, the correlation effects of d electrons of Cr atoms are quite notable. The GGA calculations of $Cr_2MC_2O_2$ give nonmagnetic ground states and nontrivial Z_2 topologies, same as the results for $Mo_2MC_2O_2$. However, the GGA+U (U $\geq$ 2 eV for Cr d electrons) calculations give magnetic ground states which break the time-reversal symmetry and then quench the QSH effects. We note that the $Cr_2MC_2O_2$ systems are the oxygen functionalized Cr_2MC_2 MXenes among which Cr_2TiC_2 has also been successfully produced by selectively etching Al atoms from the bulk MAX phase Cr_2TiAlC_2.[3]

For the practical applications, it is highly desirable to find a substrate on which the QSH states of $Mo_2MC_2O_2$ can be preserved. Since nontrivial topology of $Mo_2MC_2O_2$ arises from the $d-d$ band inversion of the TM atoms located inside $Mo_2MC_2O_2$ rather than at the surfaces, it is expected that the topological properties of $Mo_2MC_2O_2$ are insensitive to the substrate, different from the cases of silicene and bilayer Bi. Given that experimentally h-BN has been used as a good substrate to grow and support many 2D materials such as graphene,[48] MoS_2,[49] and WS_2,[50] here it is also chosen to support the $Mo_2MC_2O_2$. Taking $Mo_2HfC_2O_2$/hBN as an example, we use a 2×2 hBN cell to accommodate a $\sqrt{3} \times \sqrt{3}R30°$ $Mo_2HfC_2O_2$ cell, which reduces the lattice strain to only 3.8%, to be within the regime of strain that can be achieved experimentally for thin 2D materials. The orbital hybridization between $Mo_2HfC_2O_2$ and hBN is nearly negligible, suggesting a weak interaction between them. The electronic states of $Mo_2HfC_2O_2$/hBN near E_F at the Γ point are dominated by the $Mo_2HfC_2O_2$ and the nontrivial band topology is maintained (see Supporting Information, Figure S5), that is to say, the QSH states of $Mo_2HfC_2O_2$ are preserved on hBN. However, we also notice that, at the K point, the valence electronic states of hBN are close to E_F. This suggests hBN is still not the ideal substrate and future research may direct toward searching for a more suitable substrate than hBN.

Finally, we extend our discussion to the multilayer structures of $Mo_2MC_2O_2$. Since the $Mo_2MC_2O_2$ is exfoliated from the bulk MAX phases, the stacking order of its multilayer or the 3D bulk material is expected to be same with that in the MAX phases, as shown in Supplementary Figure S6. The binding energy of the single layer $Mo_2MC_2O_2$ to its 3D bulk phase is calculated to be 20 meV/Å^2 for $Mo_2TiC_2O_2$, 19 meV/Å^2 for $Mo_2ZrC_2O_2$, and 26 meV/Å^2 for $Mo_2HfC_2O_2$, respectively, which are slightly larger than the experimental result for graphite (12 meV/Å^2),[51] but still within the weak van der Waals coupling limit. Usually, when the single layers are stacked together to form a multilayer or 3D compound, the band gap will decrease due to the interlayer orbital coupling. In $Mo_2MC_2O_2$, the band edges (including the conduction band minimum and the valence band maximum) are contributed to by the in-plane d_{xy} and $d_{x^2-y^2}$ orbitals of the centered M atoms, rather than the orbitals of surface O atoms; therefore the electronic states of band edges show extremely weak coupling between adjacent layers, and then there is no evident band gap reduction in multilayer or 3D $Mo_2MC_2O_2$ compared to the single layer. Taking the 3D compound as an example, according to HSE calculations, the band gap is only reduced by 1 meV for $Mo_2TiC_2O_2$, 4 meV for $Mo_2ZrC_2O_2$, and 12 meV for $Mo_2HfC_2O_2$, respectively, while the decrease of band gaps for $Mo_2TiC_2O_2$ and $Mo_2ZrC_2O_2$ is negligible.

It has been shown that the multilayer Bi(111)[20] and Sb(111)[52] nanofilms, with an intermediate interlayer coupling strength, display a complex evolution of topological phases with thickness. Differently, we find the multilayer $Mo_2MC_2O_2$ films lie in the weak interface coupling regime, showing an odd−even oscillation of topological phases with thickness, i.e., trivial vs nontrivial phase for even vs odd layers, as originally predicted for adiabatically stacked 2D topological layers.[53] For this reason, the 3D bulk $Mo_2MC_2O_2$ containing two (even) layers in one unit cell (see Supplementary Figure S6) is found trivial.[54]

In summary, we demonstrate a new family of QSH insulators in single-layer $Mo_2MC_2O_2$ MXenes, which are dynamically stable, natively antioxidative, and more importantly readily feasible for experimental synthesis. TB model analysis shows

the topological orders in MXenes represent a new class of *d*-band QSH phase in a triangular lattice, which greatly expands the scope of topological materials into new lattice structures favored by metal atoms. They also represent a new type of QSH phase whose band gap is directly dictated by the SOC strength of the involving TM atoms, offering promising tunable large-gap QSH insulators. Given that the family of MXenes is quite large, more interesting topological properties in MXenes are anticipated including magnetic phases supporting quantum anomalous effect. Since Mo_2TiC_2 MXene has already been synthesized by etching Al atoms from the bulk MAX phase Mo_2TiAlC_2, with its surface oxidation controllable by high temperature annealing, it is highly reasonable to expect our theoretical prediction to be soon confirmed experimentally.

■ ASSOCIATED CONTENT

ⓢ Supporting Information

The Supporting Information is available free of charge on the ACS Publications website at DOI: 10.1021/acs.nanolett.6b03118.

> Computation methods, adsorption configurations of O on MXenes, structural stability analysis, electronic structures calculated by HSE, band structures evolution for $Mo_2HfC_2O_2$ with the increase of its thickness, and the effective two band model (PDF)

■ AUTHOR INFORMATION

Corresponding Author

*E-mail: zmsun@buaa.edu.cn.

Notes

The authors declare no competing financial interest.

■ ACKNOWLEDGMENTS

■ REFERENCES

(1) Naguib, M.; Mochalin, V. N.; Barsoum, M. W.; Gogotsi, Y. *Adv. Mater.* **2014**, *26*, 992−1005.

(2) Naguib, M.; Mashtalir, O.; Carle, J.; Presser, V.; Lu, J.; Hultman, L.; Gogotsi, Y.; Barsoum, M. W. *ACS Nano* **2012**, *6*, 1322−1331.

(3) Anasori, B.; Xie, Y.; Beidaghi, M.; Lu, J.; Hosler, B. C.; Hultman, L.; Kent, P. R. C.; Gogotsi, Y.; Barsoum, M. W. *ACS Nano* **2015**, *9*, 9507−9516.

(4) Khazaei, M.; Arai, M.; Sasaki, T.; Chung, C. Y.; Venkataramanan, N. S.; Estili, M.; Sakka, Y.; Kawazoe, Y. *Adv. Funct. Mater.* **2013**, *23*, 2185−2192.

(5) Si, C.; Zhou, J.; Sun, Z. *ACS Appl. Mater. Interfaces* **2015**, *7*, 17510−17515.

(6) Khazaei, M.; Arai, M.; Sasaki, T.; Ranjbar, A.; Liang, Y.; Yunoki, S. *Phys. Rev. B: Condens. Matter Mater. Phys.* **2015**, *92*, 075411.

(7) Guo, Z.; Zhou, J.; Si, C.; Sun, Z. *Phys. Chem. Chem. Phys.* **2015**, *17*, 15348−15354.

(8) Ling, Z.; Ren, C. E.; Zhao, M.-Q.; Yang, J.; Giammarco, J. M.; Qiu, J.; Barsoum, M. W.; Gogotsi, Y. *Proc. Natl. Acad. Sci. U. S. A.* **2014**, *111*, 16676−16681.

(9) Qi, X.-L.; Zhang, S.-C. *Phys. Today* **2010**, *63*, 33−38.

(10) Kane, C. L.; Mele, E. J. *Phys. Rev. Lett.* **2005**, *95*, 226801.

(11) Min, H.; Hill, J. E.; Sinitsyn, N. A.; Sahu, B. R.; Kleinman, L.; MacDonald, A. H. *Phys. Rev. B: Condens. Matter Mater. Phys.* **2006**, *74*, 165310.

(12) Yao, Y.; Ye, F.; Qi, X.-L.; Zhang, S.-C.; Fang, Z. *Phys. Rev. B: Condens. Matter Mater. Phys.* **2007**, *75*, 041401.

(13) Bernevig, B. A.; Hughes, T. L.; Zhang, S.-C. *Science* **2006**, *314*, 1757−1761.

(14) König, M.; Wiedmann, S.; Brüne, C.; Roth, A.; Buhmann, H.; Molenkamp, L. W.; Qi, X.-L.; Zhang, S.-C. *Science* **2007**, *318*, 766−770.

(15) Knez, I.; Du, R.-R.; Sullivan, G. *Phys. Rev. Lett.* **2011**, *107*, 136603.

(16) Liu, C.-C.; Feng, W.; Yao, Y. *Phys. Rev. Lett.* **2011**, *107*, 076802.

(17) Si, C.; Liu, J.; Xu, Y.; Wu, J.; Gu, B.-L.; Duan, W. *Phys. Rev. B: Condens. Matter Mater. Phys.* **2014**, *89*, 115429.

(18) Ma, Y.; Dai, Y.; Niu, C.; Huang, B. *J. Mater. Chem.* **2012**, *22*, 12587−12591.

(19) Xu, Y.; Yan, B.; Zhang, H.-J.; Wang, J.; Xu, G.; Tang, P.; Duan, W.; Zhang, S.-C. *Phys. Rev. Lett.* **2013**, *111*, 136804.

(20) Liu, Z.; Liu, C.-X.; Wu, Y.-S.; Duan, W.-H.; Liu, F.; Wu, J. *Phys. Rev. Lett.* **2011**, *107*, 136805.

(21) Ma, Y.; Dai, Y.; Kou, L.; Frauenheim, T.; Heine, T. *Nano Lett.* **2015**, *15*, 1083−1089.

(22) Zhou, J.-J.; Feng, W.; Liu, C.-C.; Guan, S.; Yao, Y. *Nano Lett.* **2014**, *14*, 4767−4771.

(23) Chuang, F.-C.; Yao, L.-Z.; Huang, Z.-Q.; Liu, Y.-T.; Hsu, C.-H.; Das, T.; Lin, H.; Bansil, A. *Nano Lett.* **2014**, *14*, 2505−2508.

(24) Jin, K.-H.; Jhi, S.-H. *Sci. Rep.* **2015**, *5*, 8426.

(25) Song, Z.; Liu, C.-C.; Yang, J.; Han, J.; Ye, M.; Fu, B.; Yang, Y.; Niu, Q.; Lu, J.; Yao, Y. *NPG Asia Mater.* **2014**, *6*, e147.

(26) Luo, W.; Xiang, H. *Nano Lett.* **2015**, *15*, 3230−3235.

(27) Li, L.; Zhang, X.; Chen, X.; Zhao, M. *Nano Lett.* **2015**, *15*, 1296−1301.

(28) Wang, Z.; Liu, Z.; Liu, F. *Nat. Commun.* **2013**, *4*, 1471.

(29) Qian, X.; Liu, J.; Fu, L.; Li, J. *Science* **2014**, *346*, 1344−1347.

(30) Sun, Y.; Felser, C.; Yan, B. *Phys. Rev. B: Condens. Matter Mater. Phys.* **2015**, *92*, 165421.

(31) Nie, S. M.; Song, Z.; Weng, H.; Fang, Z. *Phys. Rev. B: Condens. Matter Mater. Phys.* **2015**, *91*, 235434.

(32) Weng, H.; Dai, X.; Fang, Z. *Phys. Rev. X* **2014**, *4*, 011002.

(33) Zhou, L.; Kou, L.; Sun, Y.; Felser, C.; Hu, F.; Shan, G.; Smith, S. C.; Yan, B.; Frauenheim, T. *Nano Lett.* **2015**, *15*, 7867−7872.

(34) Li, Y.; Chen, P.; Zhou, G.; Li, J.; Wu, J.; Gu, B.-L.; Zhang, S.; Duan, W. *Phys. Rev. Lett.* **2012**, *109*, 206802.

(35) Li, Y.; Tang, P.; Chen, P.; Wu, J.; Gu, B.-L.; Fang, Y.; Zhang, S.; Duan, W. *Phys. Rev. B: Condens. Matter Mater. Phys.* **2013**, *87*, 245127.

(36) Zhou, M.; Ming, W.; Liu, Z.; Wang, Z.; Li, P.; Liu, F. *Proc. Natl. Acad. Sci. U. S. A.* **2014**, *111*, 14378−14381.

(37) Wang, Z. F.; Jin, K.-H.; Liu, F. *Nat. Commun.* **2016**, *7*, 12746.

(38) Yang, F.; Miao, L.; Wang, Z.; Yao, M.-Y.; Zhu, F.; Song, Y.; Wang, M.-X.; Xu, J.-P.; Fedorov, A. V.; Sun, Z. *Phys. Rev. Lett.* **2012**, *109*, 016801.

(39) Weng, H.; Ranjbar, A.; Liang, Y.; Song, Z.; Khazaei, M.; Yunoki, S.; Arai, M.; Kawazoe, Y.; Fang, Z.; Dai, X. *Phys. Rev. B: Condens. Matter Mater. Phys.* **2015**, *92*, 075436.

(40) Barsoum, M. W.; Radovic, M. *Annu. Rev. Mater. Res.* **2011**, *41*, 195−227.

(41) Xie, Y.; Naguib, M.; Mochalin, V. N.; Barsoum, M. W.; Gogotsi, Y.; Yu, X.; Nam, K.-W.; Yang, X.-Q.; Kolesnikov, A. I.; Kent, P. R. *J. Am. Chem. Soc.* **2014**, *136*, 6385−6394.

(42) Xie, Y.; Dall'Agnese, Y.; Naguib, M.; Gogotsi, Y.; Barsoum, M. W.; Zhuang, H. L.; Kent, P. R. C. *ACS Nano* **2014**, *8*, 9606−9615.

(43) Peng, Q.; Guo, J.; Zhang, Q.; Xiang, J.; Liu, B.; Zhou, A.; Liu, R.; Tian, Y. *J. Am. Chem. Soc.* **2014**, *136*, 4113−4116.

(44) Fu, L.; Kane, C. L. *Phys. Rev. B: Condens. Matter Mater. Phys.* **2007**, *76*, 045302.

(45) Mostofi, A. A.; Yates, J. R.; Lee, Y.-S.; Souza, I.; Vanderbilt, D.; Marzari, N. *Comput. Phys. Commun.* **2008**, *178*, 685−699.

(46) Sancho, M. L.; Sancho, J. L.; Rubio, J. *J. Phys. F: Met. Phys.* **1985**, *15*, 851.

(47) Sheng, D.; Weng, Z.; Sheng, L.; Haldane, F. *Phys. Rev. Lett.* **2006**, *97*, 036808.

(48) Yang, W.; Chen, G.; Shi, Z.; Liu, C.-C.; Zhang, L.; Xie, G.; Cheng, M.; Wang, D.; Yang, R.; Shi, D. *Nat. Mater.* **2013**, *12*, 792−797.

(49) Yan, A.; Velasco, J.; Kahn, S.; Watanabe, K.; Taniguchi, T.; Wang, F.; Crommie, M. F.; Zettl, A. *Nano Lett.* **2015**, *15*, 6324−6331.

(50) Okada, M.; Sawazaki, T.; Watanabe, K.; Taniguch, T.; Hibino, H.; Shinohara, H.; Kitaura, R. *ACS Nano* **2014**, *8*, 8273−8277.

(51) Liu, Z.; Liu, J. Z.; Cheng, Y.; Li, Z.; Wang, L.; Zheng, Q. *Phys. Rev. B: Condens. Matter Mater. Phys.* **2012**, *85*, 205418.

(52) Zhang, P.; Liu, Z.; Duan, W.; Liu, F.; Wu, J. *Phys. Rev. B: Condens. Matter Mater. Phys.* **2012**, *85*, 201410.

(53) Murakami, S. *Phys. Rev. Lett.* **2006**, *97*, 236805.

(54) Yan, B.; Muchler, L.; Felser, C. *Phys. Rev. Lett.* **2012**, *109*, 116406.